

# Spectroscopy of Ultracold, Trapped Cesium Feshbach Molecules

M. Mark,<sup>1</sup> F. Ferlaino,<sup>1,2</sup> S. Knoop,<sup>1</sup> J. G. Danzl,<sup>1</sup> T. Kraemer,<sup>1</sup> C. Chin,<sup>3</sup> H.-C. Nägerl,<sup>1</sup> R. Grimm<sup>1,4</sup>

<sup>1</sup>*Institut für Experimentalphysik and Forschungszentrum für Quantenphysik, Universität Innsbruck, 6020 Innsbruck, Austria*

<sup>2</sup>*LENS and Dipartimento di Fisica, Università di Firenze, Firenze, Italy*

<sup>3</sup>*Physics Department and James Franck Institute, University of Chicago, Chicago, Illinois 60637*

<sup>4</sup>*Institut für Quantenoptik und Quanteninformation,  
Österreichische Akademie der Wissenschaften, 6020 Innsbruck, Austria*

(Dated: June 8, 2007)

We explore the rich internal structure of Cs<sub>2</sub> Feshbach molecules. Pure ultracold molecular samples are prepared in a CO<sub>2</sub>-laser trap, and a multitude of weakly bound states is populated by elaborate magnetic-field ramping techniques. Our methods use different Feshbach resonances as input ports and various internal level crossings for controlled state transfer. We populate higher partial-wave states of up to eight units of rotational angular momentum (*l*-wave states). We investigate the molecular structure by measurements of the magnetic moments for various states. Avoided level crossings between different molecular states are characterized through the changes in magnetic moment and by a Landau-Zener tunneling method. Based on microwave spectroscopy, we present a precise measurement of the magnetic-field dependent binding energy of the weakly bound *s*-wave state that is responsible for the large background scattering length of Cs. This state is of particular interest because of its quantum-halo character.

## I. INTRODUCTION

The possibility to associate molecules via Feshbach resonances in ultracold gases [1] has opened up new avenues of research. The demonstration of coherent atom-molecule coupling [2], the creation of pure molecular samples from atomic Bose-Einstein condensates [3, 4, 5], and the formation of ultracold molecules from atomic Fermi gases [6, 7, 8, 9] paved the way for spectacular achievements. Prominent examples are the observation of molecular Bose-Einstein condensation [10, 11, 12] and the creation of strongly interacting superfluids in atomic Fermi gases [13]. Ultracold molecules have also opened up new ways to study few-body physics with ultracold atoms [14, 15]. In optical lattices, controlled molecule formation [16, 17, 18] has been the experimental key to create novel correlated states in a crystal-like environment [19, 20].

A Feshbach resonance [21, 22] arises when a bound molecular dimer state is magnetically tuned near a two-atom scattering state, leading to resonant atom-molecule coupling. The molecular structure and in particular the molecular state that interacts with the atomic threshold determine the character of a particular Feshbach resonance [1]. The rotational angular momentum of the molecular state, characterized by the rotational quantum number  $\ell$ , plays a central role. Various types of Feshbach molecules ranging from dimers in *s*-wave states ( $\ell = 0$ ) to dimers in *g*-wave states ( $\ell = 4$ ) have been realized [1].

For experiments with molecular quantum gases, cesium is particularly rich as it offers a unique variety of different Feshbach resonances and molecular states [23]. Pronounced relativistic effects lead to strong higher-order coupling between atom pairs and molecules and between different molecular states. For achieving Bose-Einstein condensation in cesium [24], the detailed understanding of the complex molecular structure was a crucial factor. The interaction properties of cesium atoms were char-

acterized by Feshbach spectroscopy in a series of atom scattering experiments performed at Stanford University [23, 25, 26]. In these experiments the magnetic field positions of many Feshbach resonances up to *g*-wave character were measured. This provided the necessary experimental input for theoretical calculations of the molecular energy structure [23, 27], performed at the National Institute of Standards and Technology (NIST). In the following, we will refer to the cesium molecular structure as presented in Ref. [23] as the “NIST model”. It represents the current knowledge of the structure of weakly bound molecular states, and thus constitutes the theoretical basis for the experiments discussed in this work.

In this Article, we report on a thorough investigation of the energy structure of weakly bound Cs<sub>2</sub> Feshbach molecules. Our experiments are performed on ultracold molecular samples confined in a CO<sub>2</sub>-laser trap [14, 28, 29, 30] and extend previous work [23] in three important ways. First, we show how any of the weakly bound molecular states can be populated based on elaborate time-dependent magnetic field control. Spectroscopy performed on various molecular states confirms the main predictions of the NIST model and provides input for further refinements of the model. Second, we demonstrate how one can indirectly populate states with high rotational angular momentum of  $\ell = 8$  (*l*-wave states) by taking advantage of avoided level crossings with  $\ell = 4$  (*g*-wave) states. For these *l*-wave states, direct Feshbach association is not feasible because of negligible coupling with the atomic scattering continuum. Third, spectroscopy on avoided crossings between bound states yields precise information about the coupling strengths between molecular states.

In Sec. II, we first review the energy structure of weakly bound Cs<sub>2</sub> dimers. In Sec. III, we address the preparation of molecular samples, detail our techniques to transfer molecular samples to various internal states, and present

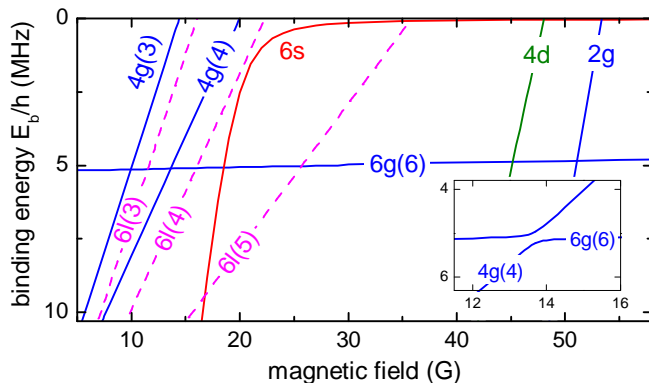


FIG. 1: (color online) Molecular energy structure below the threshold of two free Cs atoms in the absolute ground state  $|F=3, m_F=3\rangle$ . Molecular state labeling is according to the quantum numbers  $f\ell(m_f)$ ,  $m_\ell = 6 - m_f$ . The quantum number  $m_f$  is omitted for states with  $m_f = f$  and  $m_\ell = \ell$ . The solid lines represent the  $s$ ,  $d$  and  $g$ -wave states included in the NIST model [23]. The intersections of the  $d$ - and  $g$ -wave states with the threshold cause narrow Feshbach resonances that can be used for molecule production. The curvature of the  $6s$  state arises from a large avoided crossing between two states of the same  $f\ell$  quantum numbers. The NIST model does not take into account weak avoided crossings between bound molecular states mediated by the relativistic spin-spin dipole and second order spin-orbit interactions. If these interactions are taken into account, the crossings between bound molecular states become avoided as illustrated in the inset for the example of the  $4g(4)/6g(6)$  crossing. The dashed lines represent  $l$ -wave states ( $\ell = 8$ ) obtained from extended calculations based on the NIST model.

the methods for molecule detection. In Sec. IV, we report on spectroscopic measurements using magnetic moment and microwave techniques.

## II. ENERGY STRUCTURE OF WEAKLY BOUND CESIUM DIMERS

Figure 1 gives an overview of the molecular states relevant to the present work, covering the magnetic field region up to 55 G and binding energies up to  $h \times 10$  MHz, where  $h$  is Planck's constant. Zero energy corresponds to the dissociation threshold into two Cs atoms in the absolute hyperfine ground state sublevel  $|F=3, m_F=3\rangle$ . Each intersection of the atomic threshold with a molecular state corresponds to a Feshbach resonance. The rotational angular momentum associated with a molecular state is denoted by the quantum number  $\ell$ . We follow the convention of labeling states with  $\ell = 0, 2, 4, 6, 8, \dots$  as  $s, d, g, i, l, \dots$ -wave states [31] and the associated Feshbach resonances as  $s, d, g, i, l, \dots$ -wave resonances. As a consequence of the bosonic nature of Cs atoms, only even values of  $\ell$  occur. The solid lines in Fig. 1 represent states resulting from the NIST model [23], including  $s$ -,  $d$ - and  $g$ -wave states. For two interacting

TABLE I: List of angular momentum quantum numbers for the relevant molecular states. Each state is represented by four quantum numbers: the total internal angular momentum  $f$  and the rotational angular momentum  $\ell$  with  $m_f$  and  $m_\ell$  as the respective projections along the quantization axis.

label of state	$6s$	$4d$	$2g$	$4g(3)$	$4g(4)$	$6g(6)$	$6l(3)$	$6l(4)$	$6l(5)$
$f, m_f$	6,6	4,4	2,2	4,3	4,4	6,6	6,3	6,4	6,5
$\ell, m_\ell$	0,0	2,2	4,4	4,3	4,2	4,0	8,3	8,2	8,1

Cs atoms, relativistic spin-spin dipole and second-order spin-orbit interactions are particularly important [27]. Therefore, in Cs not only  $s$ - and  $d$ -wave states but also  $g$ -wave states couple sufficiently to the atomic threshold to produce experimentally observable Feshbach resonances. The magnetic field positions of these Feshbach resonances were determined experimentally in an optically confined atomic Cs gas [23, 25, 26]. The NIST predictions for the weakly bound molecular structure result from a theoretical model of the energy spectrum with parameters adjusted to reproduce the measured magnetic field positions of the Feshbach resonances.

Cs molecular states near threshold are for the most part sufficiently well characterized by the quantum numbers  $|f, m_f; \ell, m_\ell\rangle$  [1], where  $f$  represents the sum of the total atomic spins  $F_{1,2}$  of the individual atoms, and  $\ell$  is the nuclear mechanical angular momentum quantum number. The respective projection quantum numbers are given by  $m_f$  and  $m_\ell$ . In special cases the quantum numbers  $F_1$  and  $F_2$  also have to be specified. To account for the molecular structure below threshold, not only the exchange and van der Waals interaction, the atomic hyperfine structure, and the Zeeman energy, but also the weaker relativistic spin-spin dipole and second-order spin-orbit interactions have to be considered [23, 32]. The exchange and van der Waals interactions conserve  $\ell$  and  $f$ , whereas the two relativistic interactions weakly mix states with different  $\ell$  and  $f$ . The complete interaction Hamiltonian conserves the total angular momentum  $f + \ell$  at zero magnetic field. More importantly, it always conserves the projection of the total angular momentum  $m_f + m_\ell$ . In our experiments, we start with an ultracold, spin-polarized atomic sample of Cs atoms in their hyperfine ground state  $|F=3, m_F=3\rangle$ . At ultralow scattering energies only incoming  $s$ -waves ( $\ell = 0$ ) need to be considered. The atomic scattering state is hence  $|f=6, m_f=6; \ell=0, m_\ell=0\rangle$ . Consequently all molecular states relevant to the present work obey  $m_f + m_\ell = 6$ .

To label molecular states we use the three quantum numbers  $f\ell(m_f)$ . For states with  $m_f = f$  and  $m_\ell = \ell$ , we only use  $f$  and  $\ell$  for brevity. Table I gives the full set of angular momentum quantum numbers for all molecular states relevant to the present work.

Coupling between molecular states with the same  $f$  and  $\ell$  in general leads to very broad avoided crossings between molecular states. The strong curvature of the

6s state in Fig.1 is a result of such a crossing. In this case, a weakly bound 6s-state with  $F_1 = 3$  and  $F_2 = 3$  happens to couple to a 6s-state with  $F_1 = 4$  and  $F_2 = 4$ . Narrow avoided crossings arise when molecular states of different  $f$  and  $\ell$  intersect. These narrow crossings are mediated by the spin-spin dipole and second-order spin-orbit interactions. In the NIST model narrow avoided crossings were only taken into account for special cases where it was necessary to assign the experimentally observed Feshbach resonances. Consequently, the molecular states in Fig. 1 are shown as intersecting lines. Nevertheless, the existence of avoided crossings between molecular states of different  $f\ell$  is crucial for the present work as it allows the transfer of molecules from one state to another. As an example, the inset in Fig.1 schematically illustrates the avoided crossing between the  $4g(4)$  state and the  $6g(6)$  state at  $\sim 13.5$  G.

The dashed lines in Fig. 1 represent  $l$ -wave states. As states with higher angular momentum ( $\ell > 4$ ) do not couple to the  $s$ -wave scattering continuum, the  $l$ -wave states cannot be observed by Feshbach spectroscopy in an ultracold atomic gas. Consequently, no experimental input for higher angular momentum states was available for the NIST model. It is not a surprise, however, that for Cs  $l$ -wave states exist in the low magnetic field region. This follows from a general property of the asymptotic van der Waals potential [33]. In the case of an  $s$ -state being close to threshold, angular momentum states with  $\ell = 4, 8, \dots$  should also occur near threshold. The observation of both  $g$ - and  $l$ -wave states in a system with near-resonant  $s$ -wave background scattering properties nicely illustrates this general property. When the NIST model is extended to states with higher angular momentum it indeed predicts  $l$ -wave states in the low-field region [34]. The calculations are expected to accurately predict the magnetic moments, i.e. the slopes, of these states but they leave some uncertainty concerning the exact binding energies [34]. The  $l$ -wave states shown in Fig.1 result from the extended NIST model, but they are energetically adjusted to the experimental observations (Sec. IV) by equally down-shifting all three states by about  $h \times 2$  MHz.

### III. PREPARATION OF Cs<sub>2</sub> MOLECULES IN VARIOUS INTERNAL STATES

In this Section, we present our basic methods to prepare Cs<sub>2</sub> Feshbach molecules in various internal states. The starting point for all the experiments is an optically trapped ensemble of Cs atoms, the preparation of which is briefly summarized in Sec. III A. We then describe the creation of optically trapped Cs molecules based on different Feshbach resonances (Sec. III B). These resonances serve as “entrance doors” into the rich molecular structure near threshold. In Sec. III C, we discuss our techniques to transfer molecules to various internal states by application of elaborate time-variations of the

magnetic field. We make use of the possibility of adiabatic or diabatic passages through avoided crossings. In Sec. III D we discuss the methods to detect the molecular samples through controlled dissociation.

#### A. Atomic sample preparation

The setup used for the present experiments is optimized for molecule trapping and molecular state manipulation, and not for Bose-Einstein condensation (BEC) as in our previous work [3, 24, 35]. Here we start with an atomic sample near degeneracy, for which we obtain sufficient efficiencies for molecule formation.

For the present experiments we use a sequence of three dipole traps in the cooling and sample preparation process as shown in Fig. 2. The final dipole trap for molecule experiments is realized by crossing two CO<sub>2</sub>-laser beams. The far-infrared CO<sub>2</sub>-laser trap avoids the use of near-infrared radiation. In previous experiments we used the 1064-nm broad-band radiation from an Yb fiber-laser in the final trapping stage, and we observed strong light-induced trap losses for the Feshbach molecules, presumably as a result of excitation of molecular bound-bound transitions. The CO<sub>2</sub>-light is sufficiently off resonance and it thus allows for long molecule trapping times [14, 29, 30] and facilitates efficient in-trap production of molecules. One of the important features in our previous experiments on Cs BEC and the production of Feshbach molecules is the ability to levitate the atoms and molecules against gravity using a magnetic field gradient [14, 24]. However, for the preparation of molecular samples in various states the requirement of magnetic field gradients is problematic, because molecules can have widely different magnetic moments and thus require different levitation gradients. By using a relatively tight focus of one of the trapping CO<sub>2</sub>-laser beams, we can hold the molecules against gravity without the levitation gradient field.

The cooling and trapping procedure for the atoms is similar to the techniques described in Ref. [35]. In brief, we first load a magneto-optical trap (MOT) followed by a short optical molasses phase to compress and further cool the atomic sample. Using the technique of Raman sideband cooling in an optical lattice [36] the atoms are then cooled and simultaneously polarized into the lowest hyperfine state  $|F = 3, m_F = 3\rangle$ . We typically obtain  $2 \times 10^7$  atoms at a temperature of  $\sim 700$  nK.

The polarized sample is adiabatically released from the lattice into a large volume dipole trap. This “reservoir trap” is realized by two crossed laser beams. As illustrated in Fig. 2(a), we use a CO<sub>2</sub>-laser and an Yb fiber-laser for the reservoir with wavelengths of  $10.6 \mu\text{m}$  and  $1070$  nm, respectively. For each laser the beam waist is around  $650 \mu\text{m}$ . This shallow reservoir trap cannot hold the atoms against gravity. Therefore we apply magnetic levitation at this stage [24, 35]. The resulting effective trap depth is about  $7 \mu\text{K}$ . After releasing the atoms from

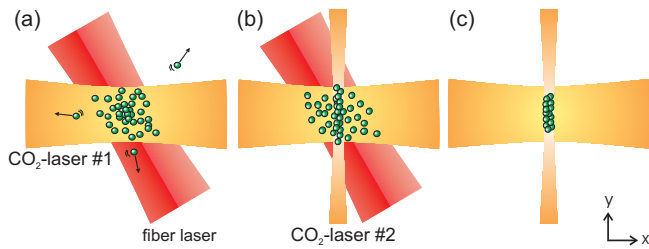


FIG. 2: (color online) Successive stages of optical dipole traps. (a) We first realize a large volume “reservoir” trap by crossing a CO<sub>2</sub>-laser beam and a 1070nm fiber-laser beam in the presence of a levitating gradient. (b) We ramp up a tightly focused CO<sub>2</sub>-laser beam, (c) switch off the 1070 nm reservoir beam and then evaporate along the vertical direction (*z*-axis) by lowering the gradient. We obtain typically  $4 \times 10^5$  Cs atoms at a temperature of 200 nK.

the optical lattice used for Raman sideband cooling into the reservoir trap, 2 s of plain evaporation are necessary to thermalize the sample in the trap. The thermalization is performed at a magnetic field of 75 G, corresponding to a scattering length of about  $1200 a_0$ , where  $a_0$  denotes Bohr’s radius. We measure about  $4 \times 10^6$  atoms at a temperature of  $\sim 1 \mu\text{K}$  [35], the phase-space density is  $\sim 1/1000$ .

After thermalization, the reservoir trap is crossed with a tightly focused CO<sub>2</sub>-laser beam as shown in Fig. 2(b). The waist of this “CO<sub>2</sub> dimple” is about  $80 \mu\text{m}$ . This value is diffraction-limited by the aperture of the window of the vacuum chamber. We linearly ramp up the power of the beam within 2.8 s to  $\sim 2.5$  W corresponding to a trap depth of about  $17 \mu\text{K}$ . Simultaneously the magnetic field is ramped down to 35 G, corresponding to a scattering length of  $700 a_0$ . This procedure provides efficient collisional loading of the CO<sub>2</sub> dimple [35]. The remaining atoms in the reservoir trap are released by switching off the Yb fiber-laser beam. In the crossed CO<sub>2</sub>-laser trap (see Fig. 2(c)) we measure typically  $1 \times 10^6$  atoms at a temperature of  $1 \mu\text{K}$ .

We then apply forced evaporative cooling by exponentially lowering the magnetic field gradient within 6.3 s to zero. Atoms thus mainly escape from the trap along the vertical direction. Simultaneously we adjust the scattering length by decreasing the magnetic field to a final value of  $\sim 22$  G to minimize three-body losses [37]. As we also slightly decrease the power of the CO<sub>2</sub> dimple to 2 W, the effective trap depth without levitation is  $\sim 2 \mu\text{K}$ .

We finally obtain  $\sim 4 \times 10^5$  Cs atoms at a temperature of about 200 nK in the crossed CO<sub>2</sub>-laser trap. The trap frequencies of the final configuration without magnetic field gradient are measured to be 84(1) Hz and 10(1) Hz in the horizontal plane, and 80(1) Hz in the vertical direction. The resulting peak density of the atoms is  $\sim 1 \times 10^{13} \text{ cm}^{-3}$ , and the phase-space density is about 0.4.

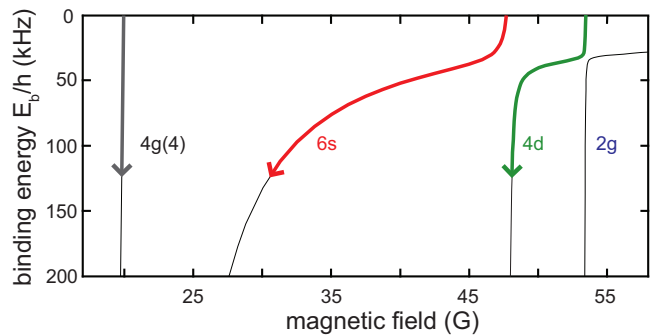


FIG. 3: (color online) The molecular energy structure for very small binding energies in the region of the 19.8 G, 47.9 G and 53.4 G Feshbach resonances, not resolved in Fig. 1. Above 45 G two avoided crossings are present in the energy structure. We use all three Feshbach resonances to associate molecules by ramping or switching the magnetic field. The arrows indicate the pathway after molecule association as the magnetic field is ramped down to allow for the optical removal of the atoms from the molecules. For details see text.

## B. Molecule production through Feshbach resonances

We magnetically associate ultracold cesium atoms to dimers on Feshbach resonances [1, 3, 4, 5]. In this work we use *three different* resonances, the two *g*-wave resonances at  $B = 19.8$  G and 53.4 G and the *d*-wave resonance at 47.9 G, see Fig. 3. The width of the *g*-wave resonances is only a few mG, the *d*-wave resonance is about 200 mG wide. While the molecule formation at the 19.8 G *g*-wave resonance results in *g*-wave molecules, the association at the 47.9 G *d*-wave resonance leads in practice to *s*-wave molecules. This is a consequence of an avoided level crossing close to threshold between the states  $4d$  and  $6s$ , see Fig. 3. Similarly, the association at the 53.4 G *g*-wave resonance results in *d*-wave molecules.

For molecule creation two different techniques are used. Depending on the character of the Feshbach resonance, we apply a ramping or a switching scheme to produce dimers [38]. The switching scheme works particularly well at the narrow *g*-wave Feshbach resonances. We set the magnetic field typically 0.5 G above the resonance. The field is then suddenly changed to the resonance position and kept there for  $\sim 5$  ms. In contrast, at the much broader 47.9 G *d*-wave Feshbach resonance we find superior efficiency by applying a linear magnetic field ramp (ramping scheme). We start typically 100 mG above the resonance and linearly ramp the magnetic field within 5 ms to about 100 mG below the resonance. The efficiencies for molecule production range from a few percent up to 20%. Starting from  $4 \times 10^5$  atoms we typically obtain 15,000 molecules, see Table II.

To prepare a maximum number of molecules in the trap, it is necessary to separate atoms and molecules as fast as possible, since atom-dimer collisions dramatically reduce the lifetime of the molecular sample [39]. We re-

TABLE II: Parameters for molecule production using three different Feshbach resonances.  $B_r$  is the field value at which the atoms are removed with the blast technique.

Feshbach resonance position (G)	19.8	47.9	53.4
entrance state	$4g(4)$	$4d$	$2g$
ramp speed (G/s)	-	36	-
state at $B_r$	$4g(4)$	$6s$	$4d$
$B_r$ (G)	14.5	19.7	45
time to reach $B_r$ (ms)	0.4	3	1
number of molecules	19000	9000	15000

move the atoms from the dipole trap using a ‘blast’ technique similar to Ref. [5]. First, the atoms are pumped out of the  $|3, 3\rangle$  state by light close to the  $F = 3 \rightarrow F' = 3$  transition. The blast pulse is tuned to the closed optical transition  $|F = 4, m_F = 4\rangle \rightarrow |F' = 5, m_{F'} = 5\rangle$ , which we also use for imaging. The optical cleaning process causes some unwanted loss and heating of the molecules. Particularly if the molecules are very weakly bound ( $\lesssim h \times 1$  MHz) or the blast duration is too long ( $\gtrsim 1$  ms) these effects are not negligible. Therefore immediately after the association we rapidly ramp the magnetic field further down. When the binding energy of the molecular state is on the order of  $h \times 5$  MHz the molecules are much less affected by the blast light. When using the 19.8 G resonance the magnetic field has to be ramped down only a few Gauss to reach such a binding energy. In case of the 47.9 G resonance (53.4 G resonance) the lowering of the magnetic field transfers the molecules into the  $6s$ -state ( $4d$ -state) through the present avoided crossings, see Fig. 3. Therefore, to reach a sufficiently large binding energy a larger change in the magnetic field is required, resulting in a longer time to reach the field. However, with a typical blast duration of  $400 \mu\text{s}$  we achieve a sufficient removal of the atoms from the trap while keeping the blast-induced molecule losses small ( $\sim 10 - 15\%$ ).

The precise timing for molecule production, the magnetic field for the purification, and the obtained number of molecules strongly depend on the particular Feshbach resonance. Table II summarizes the relevant experimental parameters of our molecule production. We measure a typical temperature of 250 nK for the molecular samples. This is slightly higher than the temperature of the atoms, presumably because of the effects of the blast cleaning technique. The corresponding peak density of the molecules is  $\sim 7 \times 10^{11} \text{ cm}^{-3}$ .

### C. Molecular state transfer

Other molecular states than the ones that we can directly access through the Feshbach creation schemes can be populated by controlled state transfer. The experimental key is the precise control of Landau-Zener tunneling at avoided crossings through elaborate magnetic field ramps. By means of the ramp speed we can choose

whether a crossing is followed adiabatically (slow ramp) or jumped diabatically (fast ramp). An important application of controlled ramps through avoided crossings is the coherent splitting of the molecular wave function for intermediate ramp speeds, as reported in Ref. [40].

Within the Landau-Zener model [41, 42] an avoided level crossing is characterized by two parameters, the coupling strength and the differential slope of the states. For the coupling strength we introduce the parameter  $V$  as half the energy splitting between the two states at the crossing point. To characterize the slope we use  $\Delta\mu$  as the magnetic moment difference between the two states. With these two parameters one commonly defines a critical ramp speed

$$r_c = \frac{2\pi V^2}{\hbar \Delta\mu}. \quad (1)$$

For fast ramps with ramp speed  $\dot{B} \gg r_c$ , the passage through the crossing is diabatic and the molecules stay in the same bare state. For slow ramps ( $\dot{B} \ll r_c$ ), an adiabatic transfer into the other molecular state takes place. For Cs Feshbach dimers the typical coupling strengths for crossings between states of different  $fl$  (see Sec. II) are such that the critical ramp speeds are found in a range convenient for experiments. Full control ranging from completely diabatic Landau-Zener tunneling to full adiabatic transfer can be achieved for most crossings (see Sec. IV A 2).

To illustrate the experimental procedure for transferring molecules into different states, we now consider the preparation of a molecular sample in a selected ‘‘target’’ state. As an example we discuss the population of the target state  $6l(4)$  in detail. As the state transfer strongly relies on the technical performance of the set-up for magnetic field control, we give a detailed description of the set-up in the Appendix .

As shown in Fig. 4(a), we first create  $4g(4)$  molecules at the 19.8 G Feshbach resonance. We then lower the magnetic field to about 14.5 G and remove the remaining atoms with the blast pulse. In a second step, see Fig. 4(b), we lower the magnetic field to  $\sim 12$  G within a few ms. Consequently, we pass the avoided crossing between the two states  $4g(4)$  and  $6g(6)$  at about 13.3 G. For this crossing the critical ramp speed, given by Eq. 1, is  $r_c \sim 1100$  G/ms as the coupling strength is  $V \simeq h \times 150$  kHz [14]. With the applied ramp speed of  $\sim 2$  G/ms the transfer into state  $6g(6)$  is therefore fully adiabatic. Fig. 4(c) illustrates the transfer of the  $6g(6)$  molecules to the target state  $6l(4)$ . First we apply a fast magnetic field ramp to overcome the  $4g(4)/6g(6)$  crossing, indicated by the straight arrow. The high ramp speed required is accomplished by a specially designed ‘‘booster’’ coil, described in the Appendix. With a maximum possible ramp speed of 7500 G/ms we achieve a transfer efficiency of typically 70%. After the jump we enter the target state  $6l(4)$  by adiabatically following the next avoided crossing between state  $6g(6)$  and  $6l(4)$  at  $\sim 15.5$  G. For this crossing we find a fully adiabatic

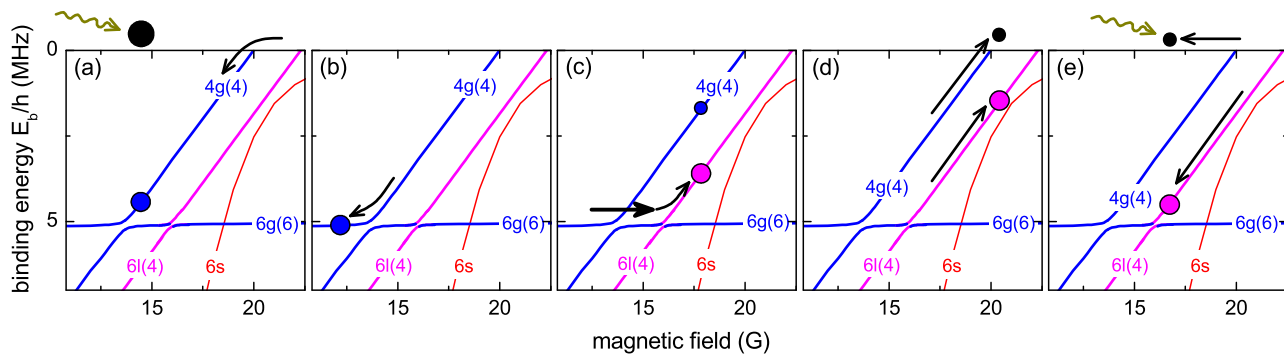


FIG. 4: (color online) Illustration of the experimental toolbox for the preparation of molecules in various internal states. As an example the creation of molecules in the  $6l(4)$  state is shown. (a) First, we produce  $4g(4)$  molecules at the  $g$ -wave Feshbach resonance at 19.8 G and remove the remaining atoms by a short blast pulse, indicated by the rippled arrow. (b) The  $4g(4)$  state is transferred into state  $6g(6)$  by slowly lowering the magnetic field. (c) To overcome the avoided level crossing between state  $4g(4)$  and  $6g(6)$  a very fast magnetic field ramp is applied. The target state  $6l(4)$  is then accessed by using a second adiabatic ramp. (d) To remove the residual  $4g(4)$  molecules from the  $6l(4)$  dimers we ramp the magnetic field slightly above 20 G, dissociating the  $4g(4)$ -molecules into atoms while not affecting the  $l$ -wave molecules. (e) The magnetic field is lowered again to increase the binding energy of the target state molecules. A second blast pulse removes the remaining atoms.

transfer when ramping the magnetic field from 15 G to  $\sim 17$  G within a few ms. In the fourth step, illustrated in Fig. 4(d), we prepare the cleaning of the sample from the residual  $4g(4)$  molecules. The magnetic field is ramped up to  $\sim 20$  G and kept constant for a few ms. While the remaining  $4g(4)$  molecules break up into atoms, the  $6l(4)$  molecules are not affected as their dissociation threshold is higher. Finally, we ramp down the magnetic field to  $B \simeq 16$  G where the target molecules are well below threshold, see Fig. 4(e). Again we remove the residual atoms using a blast pulse. As a result, we obtain a pure molecular sample in the state  $6l(4)$ .

In analogous ways, we apply these techniques to populate any of the states shown in Fig. 1.

#### D. Molecule detection

The standard detection scheme for Feshbach molecules relies on the controlled dissociation by reverse magnetic field ramps [3, 43]. When ramping the magnetic field above the dissociation threshold, the molecules become quasi-bound and decay into the atomic scattering continuum. The resulting atom cloud can then be detected using standard absorption imaging.

Magnetic dissociation by inverse magnetic field ramps is straightforward for states with large coupling to the scattering continuum, and hence any of the Feshbach resonances up to  $g$ -wave can be used. We ramp the magnetic field typically 2 G above threshold and wait a few ms at the dissociation field before the image is taken.  $l$ -wave molecules do not sufficiently couple to the atomic continuum and significant dissociation is prevented. One way to detect  $l$ -wave dimers is to transfer these molecules into one of the  $s$ -,  $d$ - or  $g$ -wave states which allow for dissociation and hence for detection.

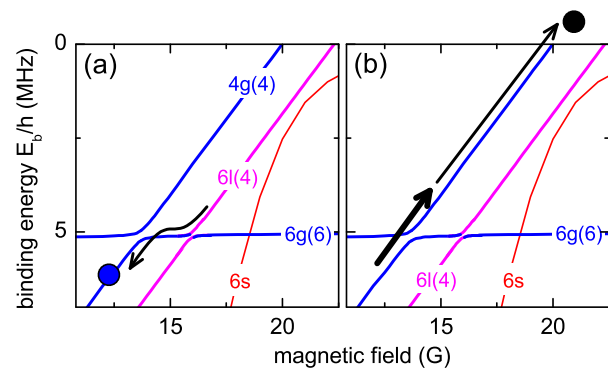


FIG. 5: (color online) Example of a detection scheme for  $l$ -wave molecules. (a) First the  $6l(4)$  molecules are adiabatically transferred into the state  $4g(4)$  via the state  $6g(6)$  by ramping down the magnetic field. (b) The avoided crossing at 13.6 G is passed by using a fast magnetic field ramp. When ramping up to a field of  $\sim 21$  G, the molecules are brought above threshold and dissociate. The resulting atom cloud is detected using the standard absorption imaging technique.

To illustrate the detection by controlled dissociation, we resume our previous example of Sec. III C, where we have described the preparation of a molecular sample in the  $6l(4)$  state. Fig. 5 shows the detection scheme that we use for this state. First the molecular sample is adiabatically transferred to the state  $4g(4)$  via the state  $6g(6)$  by lowering the magnetic field to about 12.5 G, see Fig. 5(a). We then perform a diabatic state transfer over the avoided crossing at  $\sim 14$  G as indicated in Fig. 5(b). Finally, we ramp the magnetic field up to  $\sim 21$  G, which is well above the dissociation threshold of the  $4g(4)$  state.

An alternative method for the detection of  $l$ -wave molecules relies on the particular energy structure of Cs atoms above the dissociation threshold. We find that the

decay of metastable  $l$ -wave dimers can be mediated by coupling to a quasi-bound  $g$ -wave molecular state above threshold. Such a coupling with  $\Delta\ell = 4$  is sufficiently strong. We have previously used this process for the detection of  $l$ -wave molecules in the state  $6l(3)$  in Ref. [40]. A more detailed analysis of this dissociation mechanism will be presented elsewhere [44].

For imaging of the resulting atomic cloud, the atoms are first pumped to the  $|4, 4\rangle$  state using light close to the  $F = 3 \rightarrow F' = 3$  transition. The imaging light is resonantly tuned to the closed  $|F = 4, m_F = 4\rangle \rightarrow |F' = 5, m'_F = 5\rangle$  optical transition, taking the Zeeman shift at the imaging magnetic field into account.

#### IV. FESHBACH MOLECULE SPECTROSCOPY

The rich energy structure of  $\text{Cs}_2$  Feshbach molecules requires flexible methods for determining the molecular energy spectrum. Previous studies on Feshbach molecules have mostly addressed the last, most weakly bound state responsible for the respective Feshbach resonance. Molecular binding energies have been measured by applying various methods either to atomic [2, 18, 45, 46] or to molecular samples [6, 14, 40, 47].

In this Section, we present our results on spectroscopy of weakly bound trapped molecules. We use two different techniques to measure the binding energies. Both techniques are suitable for probing weakly as well as deeply bound molecular states.

The first method (Sec. IV A) is based on a measurement of the molecular magnetic moment [14]. Magnetic moment spectroscopy is a very general method, independent of selection rules and wave function overlap requirements. It can be applied to any molecular state and thus is an important tool for molecular state identification. The method in particular allows us to follow and investigate the avoided level crossings between different molecular states. Transfers between different molecular states are observed as sudden changes of the magnetic moment. In this way, we are able to completely map out the molecular spectrum below the atomic scattering continuum, including three  $l$ -wave states, two of which had so far not been discovered.

The second method (Sec. IV B) uses microwave radiation to measure binding energies of trapped molecules with very high precision. We use a microwave pulse to drive a hyperfine transition from a molecular bound state to a higher molecular bound state that is associated with another channel of the electronic ground-state manifold. Rapid spontaneous dissociation loss [48] provides the spectroscopic signal.

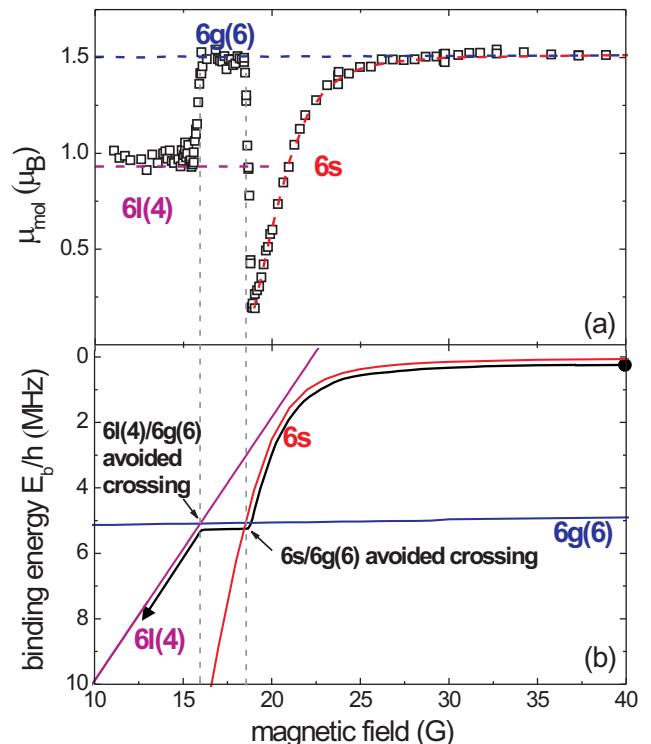


FIG. 6: (color online). Magnetic moment of Cs dimers across the  $6s - 6g(6) - 6l(4)$  molecular path. (a) The measured magnetic moments (open squares) are compared to the NIST calculations (dashed lines). The fast changes of the magnetic moment at 18.5 G and 16 G result from the  $6l(4)/6g(6)$  and  $6s/6g(6)$  avoided crossings, respectively. (b) Molecular binding energies of the  $6s$ ,  $6g(6)$  and  $6l(4)$  levels calculated from the NIST model; see also Fig. 1. The molecular path followed in the measurement is indicated by the black arrow.

#### A. Magnetic moment spectroscopy

##### 1. Bare energy levels

We measure the molecular magnetic moment using the Stern-Gerlach effect. Optically trapped molecules are initially prepared in a single quantum state at a certain magnetic field  $B$  by following the procedure described in Sec. III. The molecular sample is then released from the trap. It starts to expand while simultaneously a vertical magnetic field gradient  $B' = \partial B/\partial z$  of typically 13 G/cm is turned on. During the time of flight, both the gravitational and the magnetic force displace the center-of-mass position of the molecular cloud along the vertical direction. The magnetic force acting on the molecules is given by

$$F_z = \mu_{\text{mol}} B', \quad (2)$$

where  $\mu_{\text{mol}}$  is the molecular magnetic moment. The vertical relative displacement  $\Delta z_{\text{mol}}$  of the molecular cloud with respect to the position after expansion at zero mag-

TABLE III: Measured magnetic moment  $\mu_{\text{mol}}$  of  $\text{Cs}_2$  molecules in different internal states with the corresponding magnetic field range. The error of  $\mu_{\text{mol}}$  accounts for the statistical error and a slight change of  $\mu_{\text{mol}}$  in the range considered. For each state also the theoretical magnetic moment from the NIST model is listed.

Molecular state	$B(\text{G})$	$\mu_{\text{mol}}/\mu_B$	
		measured	NIST model
6l(3)	4 - 9	0.75(4)	0.702
	12-16	0.75(2)	0.702
4g(4)	5.5 - 12	0.95(4)	0.912
	15.5 - 20	0.949(6)	0.932
6l(4)	11 - 15	0.98(3)	0.931
	16 - 24	0.96(1)	0.931
6s	19	0.192	0.191
	45	1.519	1.515
6l(5)	15.5 - 23.5	1.15(3)	1.155
	26 - 37	1.15(2)	1.155
4d	41 - 43.2	0.39(1)	0.310
	45.5 - 47.1	0.36(2)	0.310
2g	51.7 - 52.2	0.05(3)	0.001
6g(6)	19 - 24	1.49(1)	1.503
	26 - 40	1.5(1)	1.503

netic gradient is proportional to  $\mu_{\text{mol}}$ ,

$$\Delta z_{\text{mol}} = \frac{1}{2} \frac{\mu_{\text{mol}} B'}{m_{\text{mol}}} t_{\text{SG}}^2, \quad (3)$$

where  $m_{\text{mol}} = 2m_{\text{at}}$  is the molecular mass and  $t_{\text{SG}}$  is the time spent by the molecules in the magnetic field gradient during the Stern-Gerlach procedure.

To minimize uncertainties resulting from  $B'$ ,  $t_{\text{SG}}$ , and the spatial calibration of the imaging system, it is convenient to measure  $\mu_{\text{mol}}$  relative to the well-known magnetic moment  $\mu_{\text{at}}$  of the atoms. Consequently,  $\mu_{\text{mol}}$  can be written as

$$\mu_{\text{mol}} = \frac{\Delta z_{\text{mol}}}{\Delta z_{\text{at}}} 2\mu_{\text{at}}, \quad (4)$$

where  $\Delta z_{\text{at}}$  is the measured displacement of atoms for the same  $B'$  and  $t_{\text{SG}}$ .

In previous experiments, we have determined  $\mu_{\text{mol}}$  by measuring the magnetic field gradient needed to levitate the molecules against gravity [3, 14]. For each magnetic field value  $B$ , the value of  $B'$  was adjusted to maintain the levitation condition. This method is not practical when  $B$  is changed over a wide range. In the present experiments, we measure the displacement of the molecular gas for a fixed  $B'$  and for  $B' = 0$ .

Once the magnetic moment  $\mu_{\text{mol}}$  is known as a function of  $B$ , the molecular binding energy  $E_b$  is calculated by integrating

$$\frac{\partial E_b}{\partial B} = 2\mu_{\text{at}} - \mu_{\text{mol}}. \quad (5)$$

The integration constant is fixed by the atomic scattering threshold where  $E_b = 0$ . Eq. 5 establishes a one-to-one

correspondence between  $\mu_{\text{mol}}$  and  $E_b$  at each magnetic field.

An example of a magnetic moment measurement is shown in Fig. 6. We produce  $6s$  molecules from the 47.9 G resonance, as discussed in Sec. III B. We then follow the path indicated by the arrow in Fig. 6(b) and measure the molecular magnetic moment at different values of  $B$ . We observe a strong magnetic field dependence of the magnetic moment of  $6s$  molecules. Above 30 G, where the  $6s$  level runs almost parallel to the atomic threshold (see Fig. 6(b)),  $\mu_{\text{mol}}$  is nearly constant with a value close to  $2\mu_{\text{at}}$  ( $= 1.5\mu_B$ , with Bohr's magneton  $\mu_B$ , for which  $\mu_B/h \approx 1.400 \text{ MHz/G}$ ). When lowering  $B$  below 30 G, we start to observe a decrease of  $\mu_{\text{mol}}$ , which drops to one tenth of the initial value within a magnetic field range of about 10 G. This behavior is explained by the strong coupling between two different  $6s$  states. When further lowering the magnetic field,  $\mu_{\text{mol}}$  suddenly changes from  $0.19\mu_B$  to  $1.5\mu_B$  as the molecules are transferred to the  $6g(6)$  state via the  $6s/6g(6)$  avoided crossing. The  $6g(6)$  state has a nearly constant magnetic moment, slightly less than  $1.5\mu_B$ . Upon further lowering of  $B$  the next avoided crossing (to the state  $4g(4)$ , see Fig. 1) would be expected at 13.6 G [14, 40]. However,  $\mu_{\text{mol}}$  undergoes a rapid change to a value of about  $1\mu_B$  at  $\approx 16$  G. This indicates the presence of a new avoided crossing and hence the presence of a new state. The existence of this state cannot be explained within the original NIST model [23, 27], which includes molecular states only up to  $g$ -waves. The extension of the model to higher order molecular states (Sec. II) identifies this state as a  $6l(4)$  state [34].

Similar measurements have been performed for most of the molecular states in the magnetic field range from 5 to 55 G. The results of our magnetic moment spectroscopy are summarized in Table III and the molecular energy spectrum derived using Eq. (5) is shown in Fig. 7 (open circles) along with the results of the extended NIST model (solid lines). We detect all the  $s$ ,  $d$ ,  $g$ - and  $l$ -wave states in the range of interest. Note that there are no  $i$ -wave states in this range. All  $d$ -,  $g$ - and  $l$ -wave states exhibit a rather constant magnetic moment. Consequently, we find a nearly linear dependence of the binding energy on  $B$ , as shown in Fig. 7.

In Table III and Fig. 7 we compare our results with the NIST model. In general, we find good agreement with the theoretical predictions for the binding energies and magnetic moments of the  $s$ ,  $d$  and  $g$ -wave states. The small discrepancies observed for the lower branch of the  $4g(4)$  state and for the  $4d$  state are probably the result of the more complicated production schemes introducing larger systematic errors in the measurements.

An important result of the magnetic moment spectroscopy is the detection and characterization of three  $l$ -wave states, the states  $6l(3)$ ,  $6l(4)$  and  $6l(5)$ . Recently, signatures of the  $6l(3)$  state have been reported in Ref. [40], whereas the other two states had so far not been discovered. In contrast to the  $s$ ,  $d$  and  $g$ -wave states, the

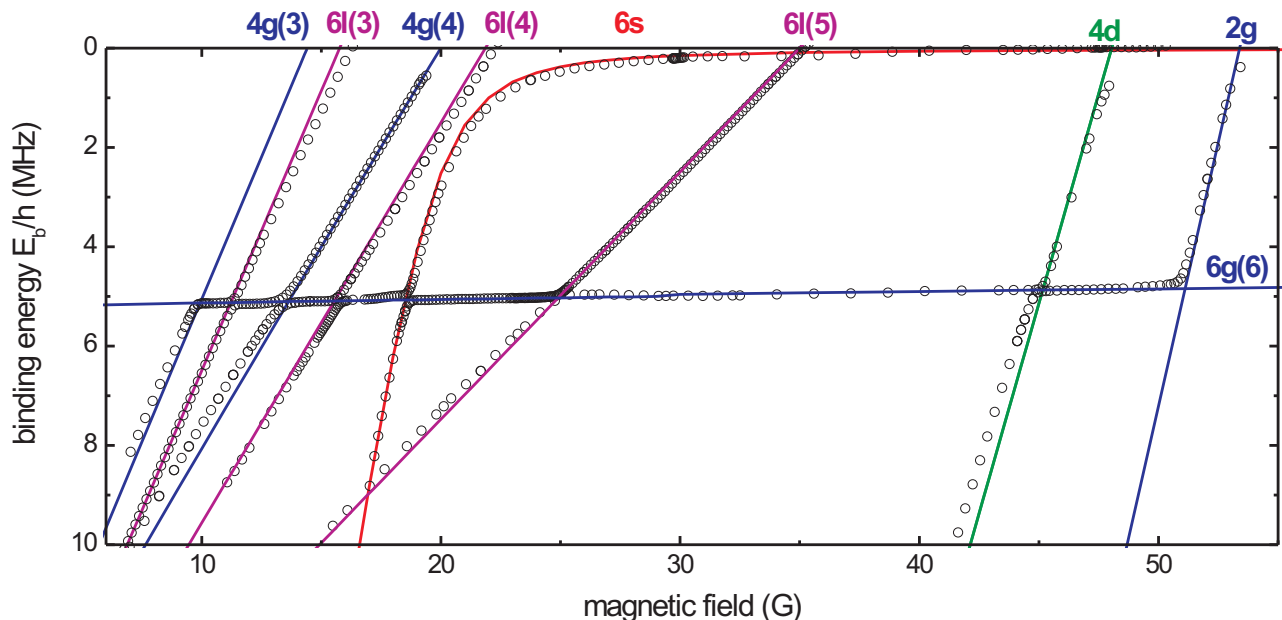


FIG. 7: (color online). Energy spectrum of weakly bound Cs molecules as a function of the magnetic field. The binding energies for the different molecular states are derived from magnetic moment spectroscopy (open circles). The solid lines are the molecular binding energies resulting from the extended NIST model (for details see Sec. II).

$l$ -wave states do not reveal themselves via Feshbach resonances in atomic scattering as the coupling to the atomic scattering state is too weak. Therefore these states had previously not been included in the NIST model. The extended NIST model shows the existence of these three  $l$ -wave states and predicts their magnetic moments. Despite the accuracy for these predictions, the model is not able to precisely determine the binding energies. Our measurements now completely characterize the three  $l$ -wave states and in particular give a value for the binding energy at zero magnetic field where all three states are degenerate. We find the binding energy of the  $6l$  manifold of states at zero magnetic field to be 17.61(9) MHz. In Fig. 1 and in Fig. 7 we have down-shifted the NIST prediction of the  $6l$  states by  $\approx 2.25$  MHz to match the experimentally obtained binding energies. The measurements also locate the magnetic field positions where the three  $6l$  states intersect the atomic scattering continuum. We find the crossing positions for the  $6l(3)$ ,  $6l(4)$ , and  $6l(5)$  states at 16.1(2) G, 22.0(2) G, and 35.0(2) G, respectively.

## 2. Avoided crossings

Magnetic moment spectroscopy also allows a direct observation of the avoided crossings between different molecular states. As is well known, the coupling  $V$  between two generic molecular states, state 1 and state 2, modifies the bare energies  $E_1$  and  $E_2$  by opening an energy gap  $2V$  at the crossing position. In the limit of a

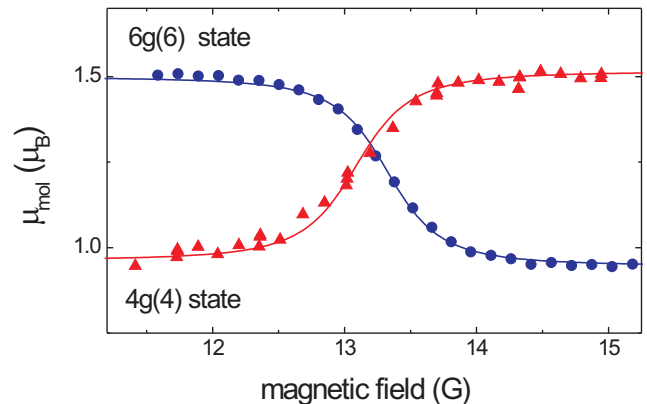


FIG. 8: (color online). Magnetic moments of Cs dimers across the  $6g(6)/4g(4)$  avoided crossing. Both the change in magnetic moment from the  $6g(6)$  to the  $4g(4)$  state (circles) and the one from the  $4g(4)$  to the  $6g(6)$  state (triangles) are shown. The measured magnetic moments are fitted using Eq. (7) (solid lines).

coupling strength  $V$  that is small compared to the energy separation to all other states, the avoided crossings can be studied within a simple two-state model. This model takes the two interacting bound states into account while both the couplings with the scattering continuum and with other molecular states are neglected. The coupled energy levels are given by

$$E_{\pm} = \frac{(E_1 + E_2) \pm \sqrt{(E_1 - E_2)^2 + 4V^2}}{2}. \quad (6)$$

TABLE IV: Avoided crossing positions  $B_0$  and coupling strengths  $V/h$  between the  $6g(6)$  state and the intersecting  $f\ell(m_f)$  molecular states obtained by fitting the measured magnetic moments with Eq. (7). The errors are the one-sigma statistical uncertainties.  $V/h$  measured with different techniques are also reported (see notes).

$f\ell(m_f)$	$B_0$ (G)	$V/h$ (kHz)
$6l(3)$	11.22(2)	$16(3)^a, 14(1)^b$
$4g(4)$	13.29(4)	164 (30) $150(10)^c$
$6l(4)$	15.50(3)	$64(13)^d$
$6l(5)$	25.3(1)	$63(22)^d$
$4d$	45.15(4)	120(21)

<sup>a</sup>Landau-Zener method.

<sup>b</sup>Interferometric method [40].

<sup>c</sup>Magnetic levitation method [14].

<sup>d</sup>The values should be considered as upper limits.

The energies  $E_+$  and  $E_-$  refer to the upper and lower adiabatic levels of the avoided crossing. The derivatives  $-\partial E_{\pm}/\partial B$  correspond to the magnetic moments  $\mu_+$  and  $\mu_-$  of the coupled states with

$$\mu_{\pm} = \frac{1}{2}(\mu_1 + \mu_2) \mp \frac{1}{2} \frac{(\mu_2 - \mu_1)^2 (B - B_0)}{\sqrt{(\mu_2 - \mu_1)^2 (B - B_0)^2 + 4V^2}}. \quad (7)$$

Here,  $B_0$  is the magnetic field at the avoided-crossing position, and  $\mu_1$  and  $\mu_2$  are the magnetic moments of the two bare molecular states.

In the following we focus on the avoided crossings between the  $6g(6)$  state and the other  $f\ell(m_f)$  states. Fig. 8 shows the magnetic moments  $\mu_+$  (circles) and  $\mu_-$  (triangles) across the  $6g(6)/4g(4)$  avoided crossing. To derive the coupling strength between these two states, we fit our data using Eq. (7) by leaving  $\mu_1$ ,  $\mu_2$ ,  $B_0$ , and  $V$  as free parameters. The same procedure is adopted to analyze the other crossings. The coupling strengths and the avoided crossing positions are listed in Table IV. For comparison, we include in Table IV measurements of  $V$  obtained with other techniques, such as the Landau-Zener method discussed below, a magnetic levitation method [14], and an interferometric method [40].

In Fig. 9 we plot the measured coupling strengths  $V$  between the  $6g(6)$  state and the other intersecting states as a function of the difference in orbital angular momentum  $|\Delta\ell|$ . While the  $6g(6)/4g(4)$  and the  $6g(6)/4d$  crossings are the result of the first order spin-spin dipole interaction, the crossings with the l-wave states are second order. As a general trend, crossings with larger  $|\Delta\ell|$  tend to have a weaker coupling.

Systematic errors in our avoided crossing measurements stem from the finite size of the molecular cloud and the change of  $\mu_{\text{mol}}$  during the free fall and expansion. These effects cause an apparent broadening of the avoided crossings and lead to an overestimation of the coupling strengths, in particular for the narrower crossings. We find a limit on the minimum coupling strength

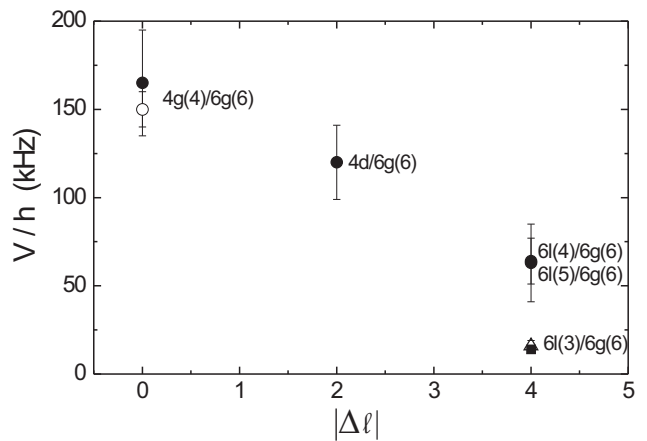


FIG. 9: Coupling strengths  $V/h$  between the  $6g(6)$  state and the intersecting  $f\ell(m_f)$  molecular states as a function of the difference their orbital angular momentum quantum numbers,  $|\Delta\ell|$ . The data refer to the values obtained via the magnetic moment spectroscopy (filled circles), a magnetic levitation method (empty circle) [14], an interferometer method (square) [40], and the Landau-Zener method (triangle).

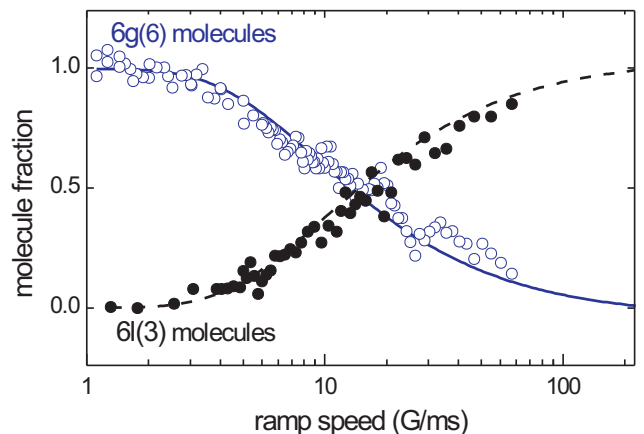


FIG. 10: (color online). Conversion efficiency on the  $6g(6)/6l(3)$  avoided crossing as a function of the ramp speed. A pure sample of  $6l(3)$  molecules is partially transferred into the  $6g(6)$  state at different ramp speeds. We measure either the fraction of transferred  $6g(6)$  molecules (open circles) or the fraction of non-converted  $6l(3)$  molecules (filled circles). The solid line refers to the Landau-Zener formula for  $p$  given by Eq. (8), while the dashed line is  $1 - p$ .

that can be extracted with reasonable precision. We estimate from simulations that coupling strengths below  $h \times 50$  kHz can no longer be sensitively measured with our present method.

An alternative method to determine the coupling strengths of avoided crossings is based on the Landau-Zener tunneling model [41, 42, 49], already discussed in Sec. III C. Eq. (1) shows a quadratic dependence of the critical ramp speed  $r_c$  on the coupling strength  $V$ . The probability to transfer molecules from one bare state to

the next in a single passage through the avoided crossing is given by the well-known Landau-Zener formula [41, 42]

$$p = 1 - \exp\left(-r_c/\dot{B}\right), \quad (8)$$

where  $\dot{B}$  is the ramp speed.

As an example, we apply this method to the  $6g(6)/6l(3)$  avoided crossing. We measure the conversion efficiency of molecules from the  $6l(3)$  state below the crossing to the  $6g(6)$  state by sweeping the magnetic field across the  $6g(6)/6l(3)$  crossing at various ramp speeds  $\dot{B}$ . The results are shown in Fig. 10. For  $\dot{B} \ll r_c$ , the molecules are adiabatically transferred to the  $6g(6)$  state (open circles) whereas, for  $\dot{B} \gg r_c$ , they end up in the  $6l(3)$  state above the crossing. The conversion efficiency is measured by detecting the  $6g(6)$  molecules (open circles) and also by detecting the  $6l(3)$  molecules (filled circles). By fitting our data with Eq. (8), we estimate the coupling strength of the  $6l(3)/6g(6)$  crossing to be  $V = h \times 16(3)$  kHz. This value is consistent with the result of  $14(1)$  kHz obtained in Ref. [40] using a more precise interferometric technique.

## B. Microwave spectroscopy

Molecules in the  $6s$  state (see Fig. 1) are of particular interest as *quantum halo* states [50]. Halo states are extremely weakly bound dimers characterized by a large interatomic separation that greatly exceeds the van der Waals length  $r_0$  (for Cs,  $r_0 \simeq 101 a_0$ ) and by a binding energy much smaller than the van der Waals energy (for Cs,  $\hbar^2/mr_0^2 \approx h \times 2.708$  MHz) [1]. These states are universal in the sense that they are fully characterized by a large atomic  $s$ -wave scattering length  $a$ . In particular, the wave function does not depend on the microscopic details of the scattering potential. The precise knowledge of the  $6s$  state is crucial for understanding universal two-body physics and for studying universal three-body Efimov-type states [15].

We detect molecular transitions induced by microwave radiation to probe the binding energy of the  $6s$  molecules. The relevant atomic states are the lowest hyperfine state  $|F = 3, m_F = 3\rangle$  and the doubly-polarized state  $|F = 4, m_F = 4\rangle$ . Fig. 11(a) shows the energy level structure of the two scattering channels  $|F = 3, m_F = 3\rangle + |F = 3, m_F = 3\rangle$  and  $|F = 3, m_F = 3\rangle + |F = 4, m_F = 4\rangle$ . The bound states involved in the molecular transition are the  $6s$  state and a  $7s$  state that lies slightly below the atomic scattering channel  $|F = 3, m_F = 3\rangle + |F = 4, m_F = 4\rangle$ .

The weakly bound  $7s$  state is directly related to the large triplet scattering length  $a_T$  that dominates the  $|F = 3, m_F = 3\rangle + |F = 4, m_F = 4\rangle$  scattering channel. The Cs triplet scattering length, predicted by the NIST model, is  $(2400 \pm 100)a_0$ , and consequently the  $7s$  state has a small binding energy of  $E'_b = \hbar^2/ma_T^2 \approx h \times 5$  kHz.

We map out the binding energy of the  $6s$  molecules by measuring the transition frequency  $\nu_{\text{mol}}$  from the  $6s$  to

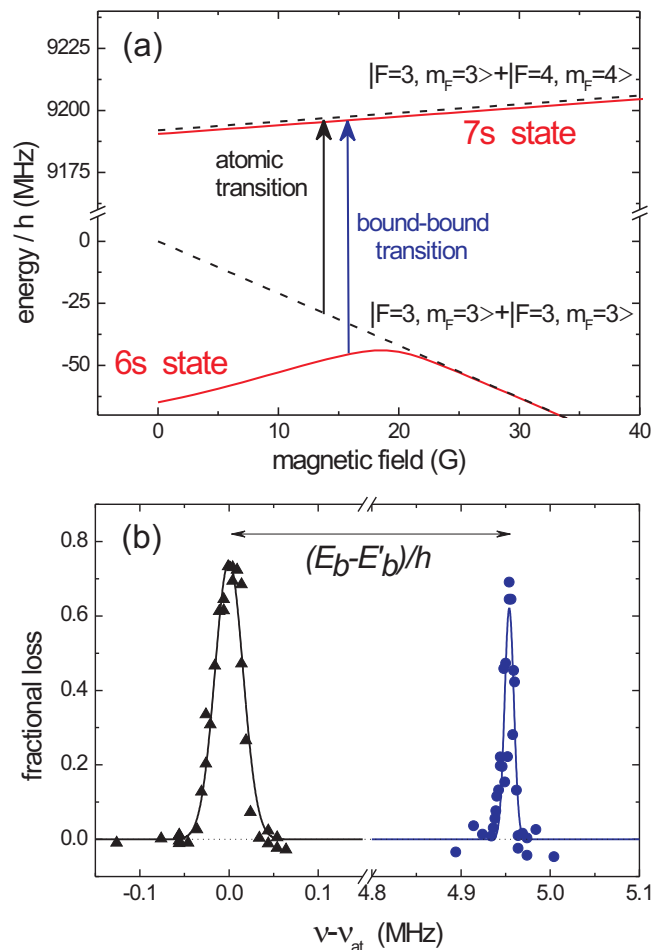


FIG. 11: (color online). Microwave spectroscopy of Cs dimers. (a) A bound-bound transition is driven from the  $6s$  state to a  $7s$  state slightly below the  $|F = 3, m_F = 3\rangle + |F = 4, m_F = 4\rangle$  scattering channel, as illustrated by the longer arrow. The  $7s$  state is offset from the scattering channel for clarity. The frequency corresponding to the  $|F = 3, m_F = 3\rangle \rightarrow |F = 4, m_F = 4\rangle$  atomic transition at zero-field is  $\nu_{\text{at}} \approx 9.193$  GHz. (b) Microwave spectrum of atoms (triangles) and  $6s$  molecules (dots) at  $B \approx 18.7$  G as a function of the frequency offset  $\nu - \nu_{\text{at}}$ . The molecular transition corresponds to a sharp loss resonance. We determine the center position to be  $4.9545(3)$  MHz and the resonance width to  $12(3)$  kHz from a gaussian fit (solid line).

the  $7s$  state as a function of  $B$ . The binding energy is then given by

$$E_b(B) = h \times (\nu_{\text{mol}}(B) - \nu_{\text{at}}(B)) + E'_b, \quad (9)$$

where  $\nu_{\text{at}}(B)$  is the  $|F = 3, m_F = 3\rangle \rightarrow |F = 4, m_F = 4\rangle$  atomic transition, which follows the Breit-Rabi formula and is used here as frequency reference. In our experiment, we again start with optically trapped  $6s$  molecules at some magnetic field  $B$ . A microwave pulse of typically 5 ms duration drives the bound-bound transition, and partially transfers molecules from the  $6s$  state to the  $7s$  state. We then hold the sample in the trap for 10 ms

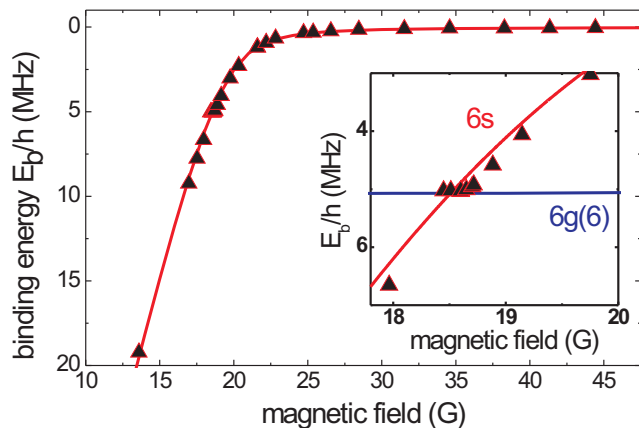


FIG. 12: (color online). Binding energy of the  $6s$  molecules as a function of the magnetic field (triangles). The binding energies correspond to the measured frequency shift from the expected  $|F=3, m_F=3\rangle \rightarrow |F=4, m_F=4\rangle$  atomic transition (see Eq. (9)). The statistical errors are about 1 kHz, i.e. much smaller than the data symbol size. The solid line is the result of the NIST model. The inset is an expanded view of the binding energy in the proximity of the  $6s/6g(6)$  avoided crossing.

and we detect the total number of remaining molecules using the techniques described in Sec. III D. We perform similar measurements at different magnetic fields to recover  $E_b$  within the magnetic field range of investigation.

As a frequency reference, we measure  $\nu_{\text{at}}(B)$  on a trapped sample of  $4 \times 10^5$  Cs atoms at  $T \approx 200$  nK, initially prepared in the hyperfine ground state  $|F=3, m_F=3\rangle$ . For each  $B$ , we apply a microwave pulse resonant to the  $|F=3, m_F=3\rangle \rightarrow |F=4, m_F=4\rangle$  hyperfine transition. The atoms are then detected after a holding time in the trap of typically 100 ms. The microwave excitation results in resonant loss from the atomic sample.

The particle losses observed in both the atomic and the molecular sample are the result of hyperfine spin relaxation [48, 51]. In the atomic case, the relaxation is driven by the binary collision of two free atoms, while in the molecular case it can be considered as being driven by a collision within the molecule [51], leading to spontaneous dissociation. In any case, one of the atoms is subject to a spin flip, releasing the hyperfine energy that greatly exceeds the trap depth and leading to trap loss. According to the NIST model, the  $7s$  state is coupled to several possible decay channels, causing a decay width of the state of  $\sim 2\pi \times 70$  Hz [34]. We in fact observe a decay of  $7s$  molecules on a timescale of a few ms. In the case of Cs atoms in the  $|F=3, m_F=3\rangle + |F=4, m_F=4\rangle$  scattering channel, we measure a lifetime of  $\sim 50$  ms consistent with the predicted two-body loss coefficient of  $5 \times 10^{-12}$  cm<sup>3</sup>/s [34].

A typical microwave spectrum for both atoms and molecules is shown in Fig. 11(b). The resonant frequencies and the line widths are determined by fitting the data with gaussian profiles. The molecular transition shows

a narrow and symmetric loss resonance. From the fit, we find a line width of 12(3) kHz. This value is close to our experimental resolution of  $\sim 10$  kHz, essentially resulting from magnetic field fluctuations. As demonstrated in Refs. [47, 52], the symmetry of line shape indicates that a bound-bound transition occurs, even in the presence of magnetic field broadening. We cannot distinguish bound-bound from possible bound-free transitions due to the small energy difference between the  $|F=3, m_F=3\rangle + |F=4, m_F=4\rangle$  scattering channel and the  $7s$  state. However, we believe that the bound-bound transition dominates as the transition probability for a bound-free transition is expected to be much weaker due to the smaller Franck-Condon overlap between the initial and final state [52].

Figure 12 shows the binding energies of  $6s$  molecules in a magnetic field range from 12 to 45 G together with the predictions from the NIST model. The inset shows an expanded view of the binding energy in the proximity of the  $6s/6g(6)$  avoided crossing at around 18.5 G. We observe an increase of the microwave power needed to drive the bound-bound transition when the avoided crossing is approached. The  $6s$  and  $6g(6)$  state couple and the molecules are in a dressed state. A microwave pulse can drive molecular transitions that change the total angular momentum  $f$  and its projection  $m_f$ , while the orbital momentum  $\ell$  has to be conserved. The bound-bound transition between the  $6g(6)$  and the  $7s$  state with  $\Delta\ell = 4$  is hence forbidden.

The microwave measurements on the  $6s$  state provide precise binding energies of up to about  $h \times 20$  MHz. Higher binding energies can in principle be accessed by further lowering the magnetic field. The comparison between our results and the NIST model generally shows very good agreement. We have observed small deviations between theory and experiment when the  $6s$  state starts to bend towards larger binding energies (see inset of Fig. 12). This deviation suggests that the  $6s$  state is perturbed by the coupling to other molecular states. Our data provide high precision input for further refinements of the NIST model.

## V. CONCLUSION

We have explored the rich internal structure of weakly bound Cs<sub>2</sub> Feshbach molecules, prepared in a CO<sub>2</sub>-laser trap. Magnetically induced association based on three different Feshbach resonances served as the entrance door into the manifold of molecular states. We have developed a set of methods to transfer molecules to various internal states, to clean the population in the optical trap from remaining atoms and from molecules in unwanted states, and to detect the molecular population via controlled dissociation. In particular, we have investigated so far unexplored  $l$ -wave states, for which direct Feshbach association is not possible because of negligible coupling to atomic scattering states.

We have determined the binding energy spectrum using two different techniques. Magnetic moment spectroscopy has been demonstrated as a versatile and sensitive method to detect molecular states. It shows avoided crossings between different molecular states and reveals the presence of higher partial wave states. Using this technique we have mapped out the molecular spectrum up to binding energies of  $E_b/h = 10$  MHz and in a magnetic field range from 5 to 55 G. Using microwave spectroscopy, we have performed highly precise measurements of the binding energy of a particularly important  $s$ -wave state above 13 G, where  $E_b/h < 20$  MHz. The results show how this state, which essentially determines the  $s$ -wave scattering length, evolves into a weakly bound state with quantum-halo character. These results are important for applications of this  $s$ -wave state to universal few-body quantum physics, such as the exploration of Efimov states.

Our measurements provide a sensitive test for the theoretical NIST model, which was developed to describe quantum scattering phenomena of Cs atoms. We could confirm the basic predictions of this model on the weakly bound molecular structure. The exploration of novel  $l$ -wave states and highly precise measurements on a weakly bound  $s$ -wave state provide experimental input for further refinements of the NIST model.

In a broader perspective, our work demonstrates general ways to manipulate Feshbach molecules through elaborate magnetic-field control. This extends the experimental tool-box available for the preparation of homo- and heteronuclear ultracold molecules in desired internal states.

### Acknowledgments

We thank E. Tiesinga, P. Julienne, and C. Williams for providing us with invaluable theoretical input and J. Hutson and A. Simoni for helpful discussions. We acknowledge support by the Austrian Science Fund (FWF) within SFB 15 (project part 16) and by the European Union within the Cold Molecules TMR Network under contract No. HPRN-CT-2002-00290. M. M. acknowledges support within the Ph.D. program DOC of the Austrian Academy of Sciences, and F. F. and C. C. within the Lise Meitner program of the FWF. S. K. is supported by the European Community with a Marie Curie Intra-European Fellowship.

### APPENDIX: MAGNETIC FIELD SETUP AND CALIBRATION

The experiments with ultracold Cs molecules are performed in a twelve-sided polygonal stainless-steel vacuum chamber with large re-entrant viewports on top and bottom for maximum optical access along the vertical axis [53]. The CO<sub>2</sub>-laser light is brought in along the horizon-

tal plane through special ZnSe-viewports. On the twelve sides of the polygon, there are in total 4 pairwise opposite viewports for the CO<sub>2</sub>-laser light and 6 pairwise opposite viewports for the near-infrared laser cooling and trapping light and for imaging. The two remaining opposite openings are reserved for the atomic beam, the Zeeman slowing laser beam, and the vacuum pumps. The total magnetic field is produced by several sets of coils, some mounted on the steel chamber, others placed inside the re-entrant viewports closer to the trap center, but still outside the vacuum. The presence of the metal limits the magnetic field switching times as a result of eddy currents. Nevertheless we achieve a maximum of experimental flexibility by combining the larger fields of the bigger coils with the more rapidly switchable fields of the smaller coils inside the viewports.

#### 1. Bias field

The vertical offset field for molecule production and manipulation is created by a pair of water cooled coils with a mean radius of 66 mm in approximate Helmholtz configuration. The coils are placed inside the re-entrant viewports along the rim of the windows. They allow a magnetic field of up to 60 G for dc-operation with a typical  $1/e$ -switching time of 1.5 ms. The current from a programmable power supply is servo-loop controlled. A second pair of large coils with a mean radius of 112.5 mm is attached to the outside of the flanges that hold the re-entrant viewports and can provide an additional dc-field of up to 200 G.

For the molecule transfer schemes as described in Sec. III, one further set of air cooled coils and a single “booster-coil” are used inside the re-entrant viewport: A pair of coils in approximate Helmholtz configuration with a radius of 44 mm is mounted on plastic holders near the vacuum window as close to the trap center as possible. The coils with a servo-loop controlled current produce a magnetic field of up to 10 G, while the  $1/e$  switching time is  $\sim 300 \mu\text{s}$ . As a result, ramp speeds in the range of 30 G/ms can be achieved. The fastest magnetic field changes are realized by a small, single “booster” coil with only 4 windings and a diameter of 24 mm at a distance of  $\sim 30$  mm to the trap center placed inside the top re-entrant viewport. Using a capacitor bench and servo-loop control for the current we achieve magnetic field pulses with amplitudes of up to 7 G. The maximum pulse duration of 1 ms is sufficiently long to adjust the offset field of the other coils within this time. With a typical switching time of 400 ns we achieve ramp speeds of up to 17000 G/ms. To change the ramp speed we vary the pulse amplitude as the rise-time cannot be adjusted. The coupling of ramp speed and pulse amplitude is somewhat problematic. It limits the possible ramp speeds at certain avoided crossings, because too large pulse amplitudes can produce uncontrolled ramps over other avoided crossings nearby. Note that the booster coil also produces a mag-

netic field gradient. However, his gradient is irrelevant for the experiments reported here.

The relative stability of the servo-loop controllers is about  $10^{-5}$  and thus well below the ambient magnetic line noise ( $\sim 10$  mG).

## 2. Gradient field

The magnetic gradient field is produced by a pair of water cooled coils in approximate anti-Helmholtz configuration. These coils with a radius of 66 mm are also placed inside the re-entrant viewports. They allow a dc-gradient field of up to 80 G/cm. Large field gradients can be switched within  $\sim 3$  ms, limited by eddy currents.

For small gradients such as 13 G/cm, as used in the magnetic moment spectroscopy measurements, we measure somewhat lower magnetic switching times of  $\sim 1$  ms.

## 3. Magnetic field calibration

To calibrate the magnetic field we use the microwave technique on a trapped atomic sample as described in Sec. IV B. We use the Breit-Rabi formula to determine the magnetic field value from a measurement of the atomic hyperfine transition frequency between the states  $|F=3, m_F=3\rangle \rightarrow |F=4, m_F=4\rangle$ . Line noise limits the stability of the magnetic field to about 10 mG for typical integration times.

- 
- [1] T. Köhler, K. Góral, and P. S. Julienne, *Rev. Mod. Phys.* **78**, 1311 (2006).
- [2] E. A. Donley, N. R. Clausen, S. T. Thompson, and C. E. Wieman, *Nature* **417**, 529 (2002).
- [3] J. Herbig, T. Kraemer, M. Mark, T. Weber, C. Chin, H.-C. Nägerl, and R. Grimm, *Science* **301**, 1510 (2003).
- [4] S. Dürr, T. Volz, A. Marte, and G. Rempe, *Phys. Rev. Lett.* **92**, 020406 (2004).
- [5] K. Xu, T. Mukaiyama, J. R. Abo-Shaeer, J. K. Chin, D. E. Miller, and W. Ketterle, *Phys. Rev. Lett.* **91**, 210402 (2003).
- [6] C. A. Regal, C. Ticknor, J. L. Bohn, and D. S. Jin, *Nature* **424**, 47 (2003).
- [7] K. E. Strecker, G. B. Partridge, and R. G. Hulet, *Phys. Rev. Lett.* **91**, 080406 (2003).
- [8] J. Cubizolles, T. Bourdel, S. J. J. M. F. Kokkelmans, G. V. Shlyapnikov, and C. Salomon, *Phys. Rev. Lett.* **91**, 240401 (2003).
- [9] S. Jochim, M. Bartenstein, A. Altmeyer, G. Hendl, C. Chin, J. Hecker Denschlag, and R. Grimm, *Phys. Rev. Lett.* **91**, 240402 (2003).
- [10] S. Jochim, M. Bartenstein, A. Altmeyer, G. Hendl, S. Riedl, C. Chin, J. H. Denschlag, and R. Grimm, *Science* **302**, 2101 (2003).
- [11] M. Greiner, C. A. Regal, and D. S. Jin, *Nature* **426**, 537 (2003).
- [12] M. W. Zwierlein, C. A. Stan, C. H. Schunck, S. M. F. Raupach, S. Gupta, Z. Hadzibabic, and W. Ketterle, *Phys. Rev. Lett.* **91**, 250401 (2003).
- [13] M. Inguscio, W. Ketterle, and C. Salomon, eds., *Ultracold Fermi Gases* (IOS Press, Amsterdam, 2007), Proceedings of the International School of Physics “Enrico Fermi”, Course CLXIV, Varenna, 20-30 June 2006.
- [14] C. Chin, T. Kraemer, M. Mark, J. Herbig, P. Waldburger, H.-C. Nägerl, and R. Grimm, *Phys. Rev. Lett.* **94**, 123201 (2005).
- [15] T. Kraemer, M. Mark, P. Waldburger, J. G. Danzl, C. Chin, B. Engeser, A. D. Lange, K. Pilch, A. Jaakkola, H.-C. Nägerl, et al., *Nature* **440**, 315 (2006).
- [16] T. Stöferle, H. Moritz, K. Günter, M. Köhl, and T. Esslinger, *Phys. Rev. Lett.* **96**, 030401 (2006).
- [17] G. Thalhammer, K. Winkler, F. Lang, S. Schmid, R. Grimm, and J. Hecker Denschlag, *Phys. Rev. Lett.* **96**, 050402 (2006).
- [18] C. Ospelkaus, S. Ospelkaus, L. Humbert, P. Ernst, K. Sengstock, and K. Bongs, *Phys. Rev. Lett.* **97**, 120402 (2006).
- [19] K. Winkler, G. Thalhammer, F. Lang, R. Grimm, J. Hecker Denschlag, A. J. Daley, A. Kantian, H. P. Büchler, and P. Zoller, *Nature* **441**, 853 (2006).
- [20] T. Volz, N. Syassen, D. Bauer, E. Hansis, S. Dürr, and G. Rempe, *Nature Phys.* **2**, 692 (2006).
- [21] E. Tiesinga, B. J. Verhaar, and H. T. C. Stoof, *Phys. Rev. A* **47**, 4114 (1993).
- [22] S. Inouye, M. R. Andrews, J. Stenger, H.-J. Miesner, S. M. Stamper-Kurn, and W. Ketterle, *Nature* **392**, 151 (1998).
- [23] C. Chin, V. Vuletic, A. J. Kerman, S. Chu, E. Tiesinga, P. J. Leo, and C. J. Williams, *Phys. Rev. A* **70**, 032701 (2004).
- [24] T. Weber, J. Herbig, M. Mark, H.-C. Nägerl, and R. Grimm, *Science* **299**, 232 (2003).
- [25] V. Vuletić, A. J. Kerman, C. Chin, and S. Chu, *Phys. Rev. Lett.* **82**, 1406 (1999).
- [26] C. Chin, V. Vuletić, A. J. Kerman, and S. Chu, *Phys. Rev. Lett.* **85**, 2717 (2000).
- [27] P. J. Leo, C. J. Williams, and P. S. Julienne, *Phys. Rev. Lett.* **85**, 2721 (2000).
- [28] T. Takekoshi, B. M. Patterson, and R. J. Knize, *Phys. Rev. Lett.* **81**, 5105 (1998).
- [29] P. Staanum, S. D. Kraft, J. Lange, R. Wester, and M. Weidemüller, *Phys. Rev. Lett.* **96**, 023201 (2006).
- [30] N. Zahzam, T. Vogt, M. Mudrich, D. Comparat, and P. Pillet, *Phys. Rev. Lett.* **96**, 023202 (2006).
- [31] H. N. Russell, A. G. Shenstone, and L. A. Turner, *Phys. Rev.* **33**, 900 (1929).
- [32] F. H. Mies, C. J. Williams, P. S. Julienne, and M. Krauss, *J. Res. Natl. Inst. Stan.* **101**, 521 (1996).
- [33] B. Gao, *Phys. Rev. A* **62**, 050702 (2000).
- [34] E. Tiesinga and P. S. Julienne, private communication (2007).
- [35] T. Kraemer, J. Herbig, M. Mark, T. Weber, C. Chin, H.-C. Nägerl, and R. Grimm, *Appl. Phys. B* **79**, 1013 (2004).
- [36] P. Treutlein, K. Y. Chung, and S. Chu, *Phys. Rev. A* **63**, 051401 (2001).

- [37] T. Weber, J. Herbig, M. Mark, H.-C. Nägerl, and R. Grimm, *Phys. Rev. Lett.* **91**, 123201 (2003).
- [38] M. Mark, T. Kraemer, J. Herbig, C. Chin, H.-C. Nägerl, and R. Grimm, *Europhys. Lett.* **69**, 706 (2005).
- [39] T. Mukaiyama, J. R. Abo-Shaeer, K. Xu, J. K. Chin, and W. Ketterle, *Phys. Rev. Lett.* **92**, 180402 (2004).
- [40] M. Mark, T. Kraemer, P. Waldburger, J. Herbig, C. Chin, H.-C. Nägerl, and R. Grimm, *subm. for publication*, arXiv:0704.0653 (2007).
- [41] L. Landau, *Phys. Z. Sowjetunion* **2**, 46 (1932).
- [42] C. Zener, *Proc. R. Soc. London, Ser. A* **137**, 696 (1932).
- [43] S. Dürr, T. Volz, and G. Rempe, *Phys. Rev. A* **70**, 031601(R) (2004).
- [44] S. Knoop, M. Mark, F. Ferlaino, J. G. Danzl, T. Kraemer, H.-C. Nägerl, and R. Grimm, *manuscript in preparation* (2007).
- [45] N. R. Claussen, S. J. J. M. F. Kokkelmans, S. T. Thompson, E. A. Donley, E. Hodby, and C. E. Wieman, *Phys. Rev. A* **67**, 060701(R) (2003).
- [46] S. T. Thompson, E. Hodby, and C. E. Wieman, *Phys. Rev. Lett.* **95**, 190404 (2005).
- [47] M. Bartenstein, A. Altmeyer, S. Riedl, R. Geursen, S. Jochim, C. Chin, J. H. Denschlag, R. Grimm, A. Simoni, E. Tiesinga, et al., *Phys. Rev. Lett.* **94**, 103201 (2005).
- [48] S. T. Thompson, E. Hodby, and C. E. Wieman, *Phys. Rev. Lett.* **94**, 020401 (2005).
- [49] P. S. Julienne, E. Tiesinga, and T. Köhler, *J. Mod. Opt.* **513**, 1787 (2004).
- [50] A. S. Jensen, K. Riisager, D. V. Fedorov, and E. Garrido, *Rev. Mod. Phys.* **76**, 215 (2004).
- [51] T. Köhler, E. Tiesinga, and P. S. Julienne, *Phys. Rev. Lett.* **94**, 020402 (2005).
- [52] C. Chin and P. S. Julienne, *Phys. Rev. A* **71**, 012713 (2005).
- [53] T. Weber, *Phd thesis*, University of Innsbruck (2003), downloadable at: [www.ultracold.at/theses](http://www.ultracold.at/theses).